

B.P Wynne, M.J. Gorley, P.F. Zheng, A.J. Cackett, M. Porton, and
E. Surrey

An analysis of the
microstructure of spark
plasma sintered and hot
isostatically pressed V 4Cr
4Ti 1.8 Y 0.4 Ti 3 SiC 2 alloy
and its thermal stability

Enquiries about copyright and reproduction should in the first instance be addressed to the Culham Publications Officer, Culham Centre for Fusion Energy (CCFE), K1/083, Culham Science Centre, Abingdon, Oxfordshire, OX14 3DB, UK. The United Kingdom Atomic Energy Authority is the copyright holder.

An analysis of the microstructure of spark plasma sintered and hot isostatically pressed V 4Cr 4Ti 1.8 Y 0.4 Ti 3 SiC 2 alloy and its thermal stability

B.P Wynne^{a,b}, M.J. Gorley^a, P.F. Zheng^c, A.J. Cackett^a, M. Porton^a, E. Surrey^a

^aUnited Kingdom Atomic Energy Authority, Culham Science Centre, Abingdon, Oxon, OX14 3DB, UK

^bDepartment of Materials Science and Engineering, The University of Sheffield, Mappin Street, S1 3JD, UK

^cFusion Reactor & Materials Division, Southwestern Institute of Physics, P.O.Box 432, Chengdu Sichuan, 610041, P.R.China

An analysis of the microstructure of spark plasma sintered and hot isostatically pressed V-4Cr-4Ti-1.8Y-0.4Ti₃SiC₂ alloy and its thermal stability

B.P Wynne^{a,b}, M.J. Gorley^a, P.F. Zheng^c, A.J. Cackett^a, M. Porton^a, E. Surrey^a

a. United Kingdom Atomic Energy Authority, Culham Science Centre, Abingdon, Oxon. OX14 3DB, UK

b. Department of Materials Science and Engineering, The University of Sheffield, Mappin Street, S1 3JD, UK.

c. Fusion Reactor & Materials Division, Southwestern Institute of Physics, P.O.Box 432, Chengdu Sichuan, 610041, P.R.China

Abstract

The microstructure and thermal stability of V-4Cr-4Ti-1.8Y-0.4Ti₃SiC₂ alloy, fabricated by 60 hr mechanical milling of blended powders followed by spark plasma sintering (SPS) and hot isostatic pressing, has been investigated. Analysis was undertaken using orientation image maps obtained from the electron backscattering and transmission Kikuchi diffraction techniques as well as hardness testing. The as-processed microstructure contained a multimodal distribution of grain sizes, in pancaked bands perpendicular to the compression axis of the SPS. This multimodal matrix grain structure exhibited regions of both random and clear <111> fibre texture with grain boundary disorientations that are virtually all high angle (>15°). Both the pancaking and texture observations are most likely a result of the long hold time of 2 hours during SPS. Post processing heat treatment showed the microstructure remained stable up to 1000°C and significant grain growth was not observed until 1200°C, suggesting this material has much potential for operation in ultra-extreme environments such as a fusion reactor.

Keywords

Vanadium; Mechanical milling; Spark plasma sintering; Multimodal microstructure; Crystallographic texture; Thermal stability

1. Introduction

A key obstacle in the optimal design and development of a commercially viable tokamak-based fusion reactor is the range of materials currently available that are low activation and can withstand the ultra extreme conditions experienced in the first wall/blanket. The blanket has multiple roles and requirements: a) convert the kinetic energy of neutrons into heat, b) extract the heat to generate power, c) produce tritium to continue the fusion reaction, and d) maintain structural integrity for at least 5 years [1]. Currently, there are no commercially available materials capable of satisfying all of these requirements and thus there is a significant technological barrier for incorporation of fusion into our energy supply systems [2].

Long term, but still on-going, evaluation of nuclear, physical, chemical and mechanical properties of possible materials for blanket applications has identified reduced activation ferritic/martensitic (RAFM) steel, oxide dispersion strengthened (ODS) steel, vanadium alloys and silicon carbide composites as attractive materials, because of their low activation status and good high temperature mechanical properties [3]. Ferritic/martensitic steels are currently the most feasible choice owing to substantial levels of development work as well significant industrial experience with such alloys in the fossil fuel and nuclear fission sectors [2-4]. A key problem with current RAFM steels such as Eurofer 97 and F82H, however, is that the temperature operating window within the anticipated conditions of the first wall/blanket is limited to approximately 350-550°C; below 350°C the material becomes brittle because of neutron damage and above 550°C the creep rates become unacceptably high [2]. Alternatively, ODS steels have the potential to increase the maximum operating temperature by several hundred degrees because of the incorporation of a fine dispersion of 2–5 nm diameter, thermodynamically stable Y, Ti and O-rich precipitates, which are uniformly distributed throughout a ferrite matrix [3]. Typically these steels are manufactured by a powder route incorporating mechanical alloying followed by various hot compaction methods (e.g. hot isostatic pressing (HIP), hot extrusion, hot pressing). In addition to concerns regarding the fabrication and welding

of these alloys, ODS steels retain some of the negative aspects of conventional RAFM steels with a noticeable reduction in strength above 500-550°C and a high ductile to brittle transition temperature in the as-manufactured form. Silicon carbide composites are promising for very high temperature operations (1500–1650°C) but there are serious issues regarding their fabrication, long-term stability and irradiation performance, particularly concerning swelling, that need to be addressed [5]. Vanadium alloys are a promising alternative to steels and silicon carbide structures; V-Cr-Ti compositions in particular have been shown to have high creep strength for long-term operation up to temperatures of 700°C, with good levels of strength and irradiation tolerance and a relatively low ductility loss because of radiation-induced defects [6, 7]. Vanadium itself is a very low activating element within the first wall/blanket environment, providing a significant advantage in decommissioning and remote handling of components [8]; however, concerns remain regarding the irradiation tolerance, tritium retention and the desirability of continuing to increase the operational design window for vanadium alloys, particularly at higher temperatures above 700°C.

Historically, vanadium has been manufactured using a wrought route, however more recently mechanical alloying (MA) has been applied to manufacture dispersion-strengthened vanadium alloys [9-12]. The pinning of dislocations by dispersed nanoparticles greatly increases strength at both ambient and elevated temperatures as well as providing enhanced thermal creep resistance and likely enhanced irradiation resistance. V, V-Ti, V-Cr, and V-W have all been studied using the MA route with Y used as a scavenger for impurities such as O and N with and without intermetallic dispersion strengthening particles such as TiC and Ti₃SiC₂ [12, 13]. Though data are limited, results indicate that the MAed vanadium-based alloys have submicron grain sizes, good tensile and better than wrought creep strength at high temperature. However, the effects of a small grain size may be an issue if diffusion enhanced grain boundary sliding is a key mechanism for promoting creep at elevated temperatures. A possible solution to this could be the production of a bimodal grain size distribution within the material, which enhances creep resistance [14] but still retains radiation-resistant, fine-grained material

with high strength and ductility at lower temperature [15-17]. One possible promising processing route to produce bimodal microstructures is spark plasma sintering (SPS) where a number of recent works have shown consolidating MA powder produces a bimodal microstructure in a range of materials including ODS steel, aluminium, and nickel [18-22]. A further added advantage of the SPS process is that it consolidates powders into bulk materials with short sintering times at low temperatures, minimising the coarsening of fine grains and nano-sized dispersed particles within the MA powders [23].

The aim of the present work thus was to characterize a V-4Cr-4Ti-1.8Y-0.4Ti₃SiC₂ alloy material produced by MA of pure elemental powders with YH₂ and Ti₃SiC₂ followed by compaction via SPS plus HIP to ensure 100% density. Microstructure analysis for the as-compacted material was primarily conducted using the electron backscattering diffraction (EBSD) technique in a scanning electron microscope. Particular focus was paid to analysis of the matrix grain structures, grain boundary disorientation distribution and crystallographic textures, as well as their thermal stability in the expected operation temperatures of commercial fusion reactor.

2. Experimental Procedure

The starting material consisted of elemental powders of vanadium (99.9%, 200 mesh), chromium (99.7%, 200 mesh), titanium (99.4%, 200 mesh), and yttrium hydride (99.95%, 75 mesh) supplied by Liaoyuan Non-ferrous Alloy Plant, China and Ti₃SiC₂ powder supplied by Wuhan University of Technology, China. The powders were mixed in an argon atmosphere prior to mechanical milling (MM) to a nominal composition of V-4Cr-4Ti-1.8Y-0.4Ti₃SiC₂ (wt%) with the yttrium content chosen on the assumption it would scavenge most of the O and N impurities to form yttrium oxide and nitride. MM was undertaken using yttria-stabilized zirconia balls of 5 mm diameter together with approximately 50 g of the mixed powder (ball-to-material weight ratio was 7:1) in a sealed yttria-stabilized zirconia pot filled with argon. Mechanical milling was performed at room temperature using a Q5SP-4L milling machine at 300 rpm for milling times ranging from 0.5 to 120 hrs

to identify the optimum milling time. An X-ray diffractometer (X' Pert PRO, PANalytical B.V., Netherlands with a wavelength $\lambda = 0.15405$ nm) was used to record the x-ray diffraction patterns of the milled powders to determine the optimum milling time. Approximately 200 g of as-milled powder from 10 batches was then consolidated in a two stage process: firstly by spark plasma sintering (SPS) under 35 MPa at 1150 °C for 2 hr followed by HIPing at 1100°C, under 150 MPa, for 2.5 hr. This produced two disks of 160 mm in diameter and 7~9 mm thick.

To investigate the thermal stability of the microstructure, 10 mm x 10mm x 7 mm samples were cut from the as-HIPed material from a region at approximately 2/3 radius of the disk and sealed in argon filled glassed tubes, heated in a tube furnace at 600, 700, 800, 1000, and 1200°C for 2 hrs, respectively, and then air cooled. The Vickers hardness of each specimen was measured with a Vickers hardness tester using an applied load of 1 kg and a dwell time of 15 seconds. Microstructure analysis was undertaken for the as-HIPed and heat-treated specimens in a plane parallel to the SPS compression direction at the mid section, using high-resolution EBSD. Acquisition of EBSD data was undertaken using a TESCAN Mira3 XMH field-emission gun scanning electron microscope (SEM) equipped with a fully automatic Oxford Instruments AZtec EBSD attachment, and operated at 20 kV using a step size of 0.1 μm . Higher resolution microstructure analysis was undertaken by Transmission Kikuchi Diffraction (TKD). The thin foils used for TKD were produced using a FEI Helios 600 NanoLab dual beam SEM/FIB equipped with a gallium ion source. To avoid surface damage during FIB milling, i.e. Ga ion implantation, platinum was first deposited on the surface. FIB milling was performed at 30kV, 80pA to start, with successively lower beam voltages and currents (16kV, 50pA; 8kV, 66pA) down to 5kV, 41pA for the final clean to further reduce surface damage. TKD analysis was performed using the same equipment as the EBSD with an accelerating voltage of 30 kV using a step size of 0.012 μm .

3. Results

Figure 1 shows the x-ray traces of the as-MMed powder as a function of milling time. At approximately 70 hr, a near complete solid solution of Ti and Cr in V is achieved, beyond which there is clear evidence of ZrO₂ contamination from the milling media. Note, the volume fraction of Ti₃SiC₂ particles was too small to be observed. Thus 60 hours was chosen as the milling time for the materials to be consolidated assuming that the remaining alloying elements would dissolve during subsequent sintering and with minimal chance of ZrO₂ contamination.

Figure 2 displays the hardness of the as-processed and heat-treated materials. From the as-processed material up to material exposed to 1000°C the hardness is very stable, with a slight increase from 270 to 280 Hv, suggesting the microstructure is stable up to 1000°C. At 1200°C there is a significant increase in hardness to 320 Hv, suggesting that there has been either a significant precipitation event or possible take-up of residual interstitials from the argon filled glass chamber.

Figures 3a and b show example EBSD orientation images (OIM) and band contrast maps obtained from the vanadium matrix of the as-HIPed material, respectively. Both maps show a microstructure containing layers of pancaked bands consisting of contiguous similar sized grains, which lie near perpendicular to the applied compression direction (Z) of the SPS. There appears to be 3 band types: bands consisting of grains with sizes ranging from 1 to 4 μm, bands with grain sizes of the order 0.4 to 1 μm and bands with grains too small to be detected using standard EBSD, as highlighted by the band contrast map. To investigate the grain size within the non-detectable bands, a TKD map of one of these bands is shown in Figure 3c. Again not all areas could be indexed but it is clear that that grain size range is in the order of 0.05 to 0.4 μm.

In the vast majority of cases investigated (8 maps were investigated), the pancaked bands lie perpendicular to the compression axis of the SPS. This would suggest that the SPS played the key role in determining the formation of the bands, as the isotropic

HIP process should generate a random spatial distribution of grains.

Figures 3d and e show {111} pole figures from standard EBSD analysis of the region shown in Figure 3a and from another dataset collected in a similar region in the same sample, respectively. The pole figures display a texture variation seen throughout the analysis; some regions have a relatively random texture, as would be expected from a relatively fast sintering of a random powder [21], whilst other regions display a distinct <111> fibre texture centered on the compression direction, as would be expected from large strain uniaxial compression of a BCC polycrystal [24]. It should be noted, there appeared to be no significant morphological differences between the different textured regions, with both having similar pancaked grain groupings. Again, this would suggest the SPS, with its uniaxial loading, had the biggest impact on the microstructure, as a completely random texture would be expected from HIPing. Analysis of boundary disorientation in the OIMs shows that the vast majority to be of high angle (>15°) for all bands, with occasional pockets of low angle boundaries. This is statistically confirmed in Figure 3f, which shows the distribution of boundaries for the datasets shown in Figures 3d and e.

Representative OIMs and associated {111} pole figures for the 800, 1000, and 1200°C heat-treated material are shown in Figure 4. These data indicate that up to 1000°C the microstructure is highly stable with no obvious change in any of the banded structures, whilst at 1200°C abnormal grain growth appears to have occurred in localised pockets, but there is still evidence throughout the microstructure of the 3 banded structures. There also appears to be no impact of the different texture regions on microstructure stability as clearly shown in Figures 4a and d. Note, the texture for the 1200°C material shown in Figure 4i is very strong because of the very large abnormal grain within the EBSD map. Regions outside this grain display the as-processed random distribution of orientations.

4. Discussion

In terms of the observed as-processed microstructure, the results presented here are in good agreement with those of Kubota and Wynne for a nanocrystalline Al fabricated from a combination of MM and SPS [21]. In their EBSD analysis they found a bimodal distribution of coarse and fine grains with sizes of 2–5 μm and 300 nm, respectively, which was produced from a powder with an average grain size of 38 nm, while in the current case there is a multimodal distribution of grain sizes, which are in approximate size groupings of 0.05 to 0.4 μm , 0.4 to 1 μm , and 1 to 4 μm . It was suggested [21] that the coarse grains were formed by localized high temperatures generated at the start of the SPS process as current paths are restricted to localized contact points between grains before densification begins. On the other hand, the finer grain size observed in the OIM can be explained by grain boundary pinning by Ti_3SiC_2 particles, as generally suggested in the literature [25,26]. Some aspects of the morphology of the microstructure and the crystallographic texture are, however, different from what is normally presented from SPS processing, namely pancaked clusters of grains that lie close to perpendicular to the compression axis and regions that exhibit a strong $\langle 111 \rangle$ fiber texture parallel to the compression axis. Both these observations suggest that the applied load during SPS was a significant factor in influencing microstructure development. In hindsight, this is not unexpected given that unlike typical SPS processing times of 5 to 10 minutes, the hold time during SPS was two hours, suggesting that the processing was more akin to SPS assisted uniaxial hot pressing, i.e. the material experienced significantly more deformation than standard SPS processing. Interestingly, this long hold time had no major influence on grain size, implying the Ti_3SiC_2 particles were very effective at pinning grain boundaries. The fact that most grains are in pancaked clusters and are relatively strain free, delineated by high-angle boundaries, indicates the grains have been deformed and then have undergone recrystallisation until being pinned by the Ti_3SiC_2 particles or have been deformed very slowly, such that the rate of recovery is sufficiently high that there is minimal substructure development for the formation of subgrains. Moreover, the variation in texture from random levels to clear $\langle 111 \rangle$ fibre texture suggests that regions

within the material have experienced different levels of deformation ranging from sufficient to change shape but not have a significant impact on grain orientation distribution, through to enough deformation to generate a clear texture. Regions being sintered to different levels of density may explain this; where the current density is high there will be rapid sintering forming effective hard dense regions, while in other regions that are less dense there will be more deformation accommodated by the greater level of free volume, leading to variable levels of permanent deformation. It is therefore interesting to note that there was no major evidence to suggest that the grain size was significantly different in the different texture regions, again indicating the Ti_3SiC_2 particles determined the grain size distribution, regardless of the level of deformation experienced. This also signifies that the Zener pinning pressure [27] generated by the volume fraction and size of Ti_3SiC_2 particles used is sufficiently high enough to stabilize a fine grain size up to 1150°C .

From analysis of the as-processed material it is unsurprising that there is microstructure and hardness stability up to 1000°C , as 1. the recrystallization temperature for vanadium alloys is usually greater than 950°C , and even higher if impurities are introduced [28,29], and 2. the microstructure has effectively been double stabilized by the long hold times at the higher temperatures of the SPS (1150°C) and HIPing (1100°C) processes. At 1200°C it is clear that some abnormal grain growth occurs, indicating that the Zener pinning pressure of the Ti_3SiC_2 particles is not sufficient, at least for certain grain disorientations, to maintain microstructure stability at 1200°C . The increase in hardness at 1200°C does not appear to be related to grain size but to other factors including precipitation of additional phases or uptake of interstitials, which at this stage cannot be determined without more detailed analysis, outside the scope of this current investigation.

5. Conclusions

In summary, the combination of MM, long hold time SPS and HIP processes has been used successfully to fabricate bulk, fully dense, fine-grained V-4Cr-4Ti-1.8Y-0.4 Ti_3SiC_2

alloy. The microstructure of the as-processed material possesses a multimodal distribution of grain sizes, which are distributed in pancaked bands, most likely produced during the long hold time during SPS, perpendicular to the compression axis of the SPS in approximate size groupings of 0.05 to 0.4 μm , 0.4 to 1 μm , and 1 to 4 μm . The Ti_3SiC_2 particles appear to have sufficient Zener pinning capability at the SPS processing temperature of 1150°C to lead to high thermal stability of the microstructure to at least 1000°C. This shows vanadium alloys with combined thermally stable Ti_3SiC_2 particles and processed to be thermally stable at high temperatures have much potential to operate in extreme environments, such as a fusion reactor.

6. Acknowledgement

This work made use of equipment at the Materials Research Facility at the United Kingdom Atomic Energy Authority, which was funded as part of the UK National Nuclear User Facility. The work has been funded by the RCUK Energy Programme [grant number EP/I501045]. To obtain further information on the data and models underlying this paper please contact PublicationsManager@ccfe.ac.uk.

7. References

- [1] A.R. Raffray, M. Akib, V. Chuyanov, L. Giancarli, S. Malang, Breeding blanket concepts for fusion and materials requirements, *J. Nucl. Mater.* 307–311 (2002) 21–30.
- [2] M.J. Gorley, Critical Assessment 12: Prospects for reduced activation steel for fusion plant, *Mater. Sci. Technol.* 31 (2015) 975–980.
- [3] S.J. Zinkle, Advanced materials for fusion technology, *Fusion Eng. Des.*, 74 (2005) 31–40.
- [4] R.L. Klueh, Ferritic/martensitic steels for advanced nuclear reactors, *T. Indian I. Metals*, 62 (2009) 81–87.
- [5] L.L. Snead, T. Nozawa, M. Ferraris, Y. Katoh, R. Shinavski, M. Sawan, Silicon carbide composites as fusion power reactor structural materials, *J. Nucl. Mater.* 417 (2011) 330–339.
- [6] D.L. Smith, H.M. Chung, B.A. Loomis, H.-C. Tsai, Reference vanadium alloy V4Cr4Ti for fusion application, *J. Nucl. Mater.* 233–237 (1996) 356–363.
- [7] J.M. Chen, V.M. Chernov, R.J. Kurtz, T. Muroga, Overview of the vanadium alloy researches for fusion reactors, *J. Nucl. Mater.* 417 (2011) 289–294.
- [8] M.R. Gilbert, J.-Ch. Sublet, R.A. Forrest, Handbook of activation, transmutation, and

radiation damage properties of the elements simulated using FISPACT-II & TENDL-2014; Magnetic Fusion Plants” Tech. Rep. CCFE-R(15)26, CCFE, available to download from http://www.ccf.ac.uk/fispact_handbooks.aspx (2015).

[9] T. Sakamoto, H. Kurishita, S. Kobayashi, K. Nakai, High temperature deformation of V-1.6Y-8.5W-(0.08, 0.15)C alloys, *J. Nucl. Mater.* 386–388 (2009) 602–605.

[10] T. Furuno, H. Kurishita, T. Nagasaka, A. Nishimura, T. Muroga, T. Sakamoto, S. Kobayashi, K. Nakai, S. Matsuo, H. Arakawa, Effects of grain size on high temperature creep of fine grained, solution and dispersion hardened V–1.6Y–8W–0.8TiC, *J. Nucl. Mater.* 417 (2011) 299–302.

[11] H. Kurishita, S. Oda, S. Kobayashi, K. Nakai, T. Kuwabara, M. Hasegawa, H. Matsui, Effect of 2 wt% Ti addition on high-temperature strength of fine-grained, particle dispersed V–Y alloys, *J. Nucl. Mater.* 367–370 (2007) 848–852.

[12] T. Sakamoto, H. Kurishita, T. Furuno, T. Nagasaka, S. Kobayashi, K. Nakai, S. Matsuo, H. Arakawa, A. Nishimura, T. Muroga, Uniaxial creep behavior of nanostructured, solution and dispersion hardened V–1.4Y–7W–9Mo–0.7TiC with different grain sizes, *Mater. Sci. Eng. A* 528 (2011) 7843–7850.

[13] P.F. Zheng, T. Nagasaka, T. Muroga, J.M. Chen, Investigation on mechanical alloying process for vanadium alloys, *J. Nucl. Mater.* 442 (2013) S330–S335.

[14] S. Onaka, Deformation behavior and stress states of a diffusional creeping polycrystal with bimodal grain-size distribution, *Arch. Mech.* 62 (2010) 241–251.

[15] B.N. Singh, Effect of grain size on void formation during high-energy electron irradiation of austenitic stainless steel. *Philos. Mag.* 29 (1974) 25–42.

[16] S. Ukai, M. Fujiwara, Perspective of ODS alloys application in nuclear environments. *J. Nucl. Mater.* 307–311 (2002) 749–757.

[17] O. El-Atwani, D.V. Quach, M. Efe, P.R. Cantwell, B. Heim, B. Schultz, E.A. Stach, J.R. Groza, J.P. Allain, Multimodal grain size distribution and high hardness in fine grained tungsten fabricated by spark plasma sintering, *Mater. Sci. Eng. A* 528 (2011) 5670–5677.

[18] Ch.Ch. Eiselt, M. Klimenkov, R. Lindau, A. Möslang, H.R.Z. Sandim, A.F. Padilha, D. Raabe, High-resolution transmission electron microscopy and electron backscatter diffraction in nanoscaled ferritic and ferritic–martensitic oxide dispersion strengthened steels, *J. Nucl. Mater.* 385 (2009) 231–235.

[19] I. Hilger, F. Bergner, T. Weißgärber, Bimodal Grain Size Distribution of Nanostructured Ferritic ODS Fe–Cr Alloys, *J. Am. Ceram. Soc.* 98 (2015) 3577–3581.

[20] H. Zhang, Y. Huang, H. Ning, C.A. Williams, A.J. London, K. Dawson, Z. Hong, M.J. Gorley, C.R.M. Grovenor, G.J. Tatlock, S.G. Roberts, M.J. Reece, H. Yan, P.S. Grant, Processing and microstructure characterisation of oxide dispersion strengthened Fe–14Cr–0.4Ti–0.25Y₂O₃ ferritic steels fabricated by spark plasma sintering, *J. Nucl. Mater.* 464 (2015) 61–68.

[21] M. Kubota, B.P. Wynne. Electron backscattering diffraction analysis of mechanically milled and spark plasma sintered pure aluminium, *Scr. Mater.* 57 (2007), 719–722.

[22] D. Tingaud, P. Jenei, A. Krawczynska, F. Momprou, J. Gubicza, G. Dirras, Investigation of deformation micro-mechanisms in nickel consolidated from a bimodal powder by spark plasma sintering, *Mater. Charact.* 99 (2015) 118–127.

[23] Z.A. Munir, D.V. Quach, M. Ohyanagi, Electric Current Activation of Sintering: A

- Review of the Pulsed Electric Current Sintering Process, *J. Am. Ceram. Soc.* 94 (2011) 1-19.
- [24] U.F. Kocks, C.N. Tomé, H. -R. Wenk, *Texture and Anisotropy: Preferred Orientations in Polycrystals and their Effect on Materials Properties*, Cambridge University Press, Cambridge, UK, 2000.
- [25] A. Eldesouky, M. Johnsson, H. Svengren, M.M. Attallah, H.G. Salem, Effect of grain size reduction of AA2124 aluminum alloy powder compacted by spark plasma sintering, *J. Alloy Compd.* 609 (2014) 215–221.
- [26] H. Chen, B. Yang, Effect of Precipitations on Microstructures and Mechanical Properties of Nanostructured Al-Zn-Mg-Cu Alloy, *Mater. T. JIM*, 49 (2008). 2912- 2915.
- [27] C.S. Smith, Grains, phases, and interphases: an interpretation of microstructure, *Trans. metall. Soc. A.I.M.E.*, 175 (1948) 15-51.
- [28] J. Chen, T. Muroga, T. Nagasaka, Y. Xu, S. Qiu, The recovery and recrystallization of cold rolled V–W–Ti alloys, *J. Nucl. Mater.* 322 (2003) 73–79.
- [29] N.J. Heo, T. Nagasaka , T. Muroga, Recrystallization and precipitation behavior of low-activation V–Cr–Ti alloys after cold rolling, *J. Nucl. Mater.* 325 (2004) 53–60.

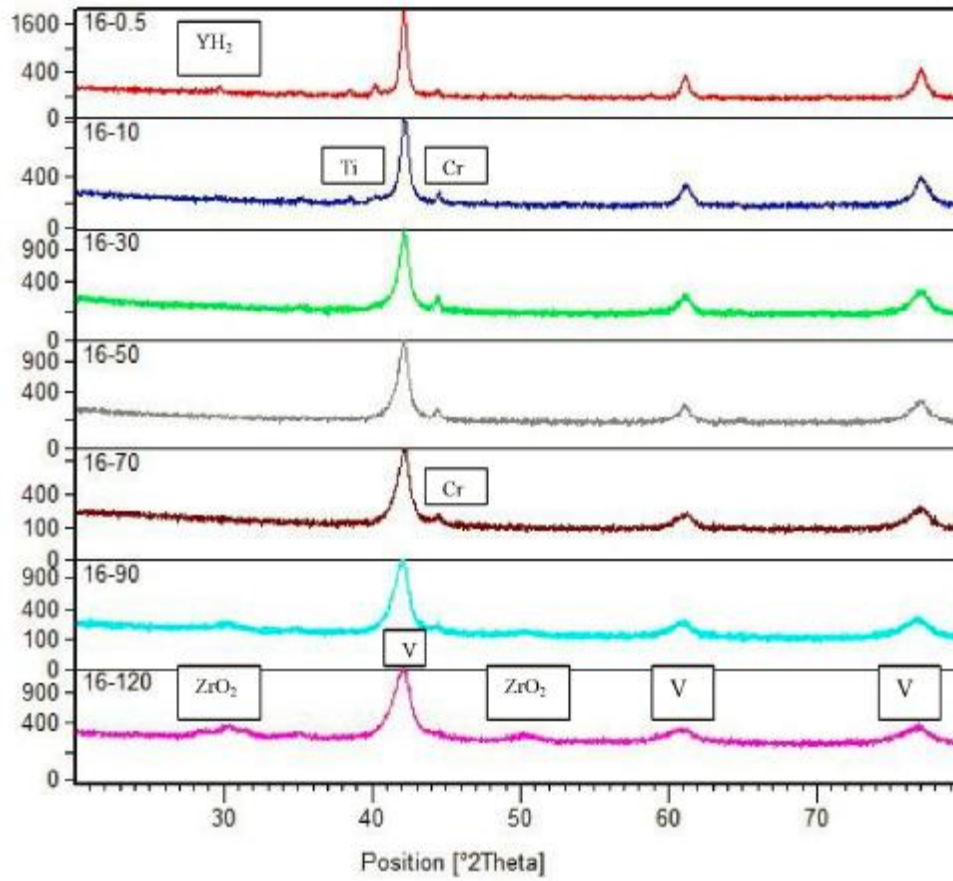


Figure 1. X-ray traces of as mechanically milled powder ranging in times from 0.5 to 120 hours.

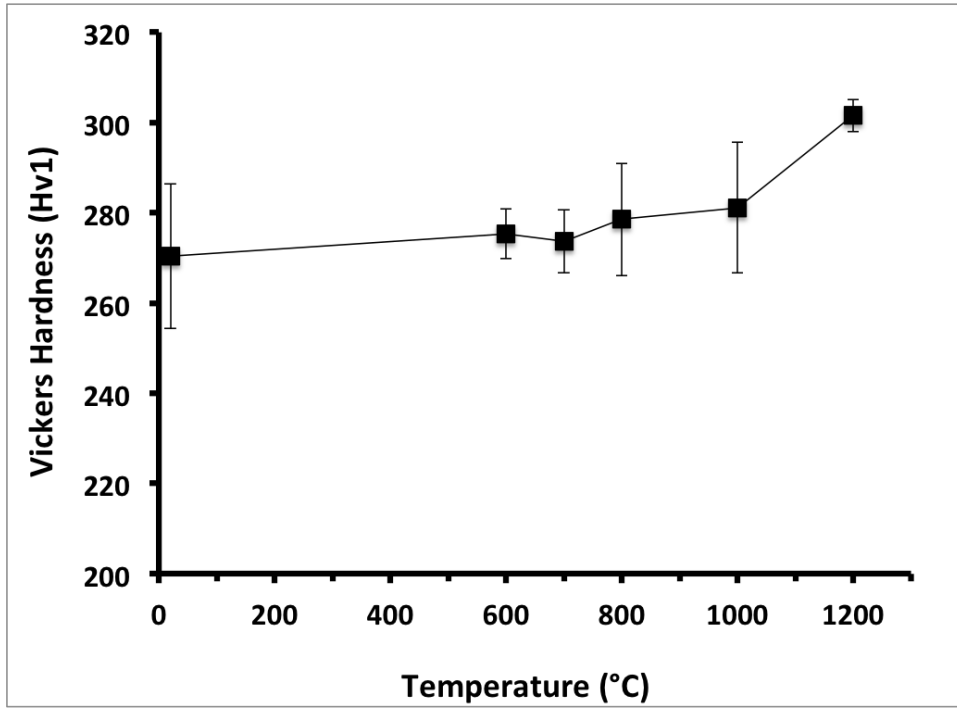


Figure 2. Hardness of as-processed and heat treated material as a function of heat treatment temperature.

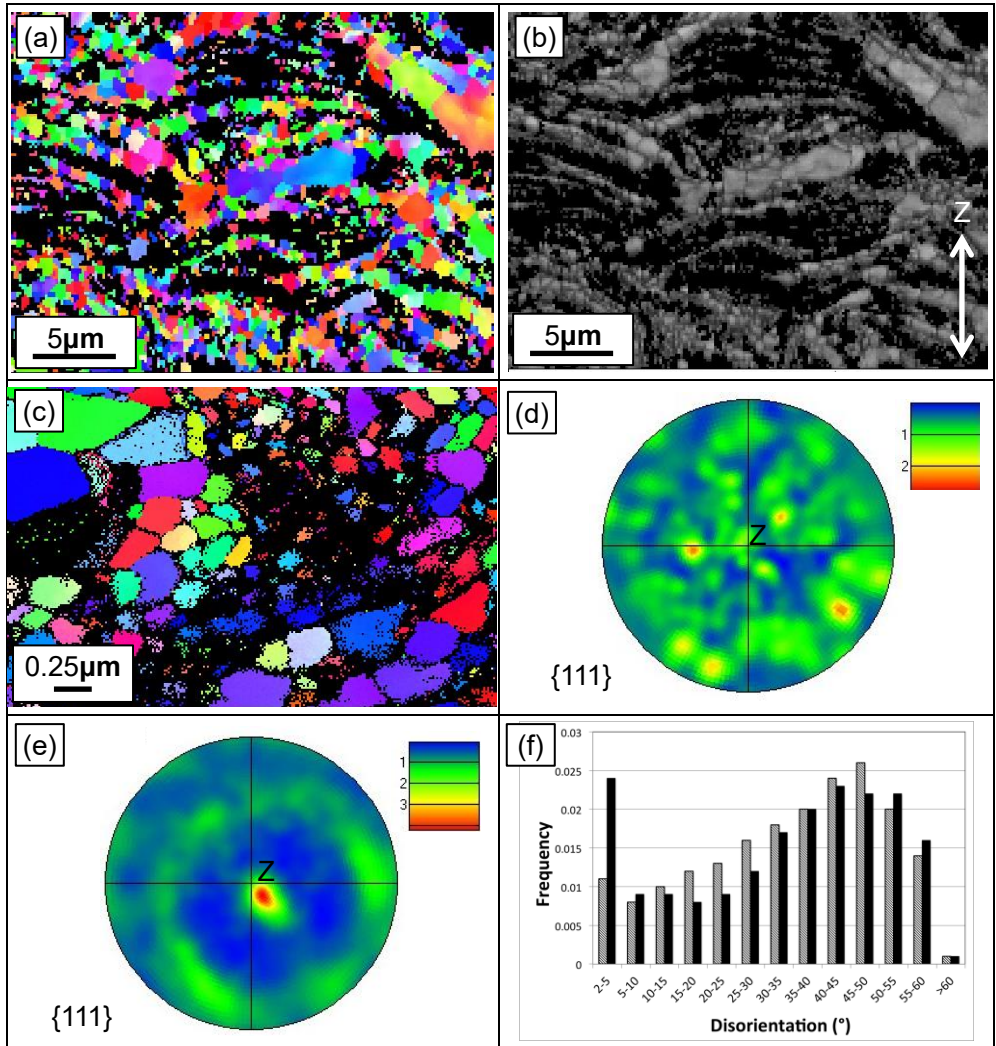


Figure 3. EBSD data of as-processed material (a) Inverse pole figure (IPF) map of as-processed material, (b) band contrast image of (a), (c) high resolution TKD map of fine-grained region, (d) {111} pole figure of (a), (e) {111} pole figure of a region close to (a). (f) Distribution of disorientation axes for pole figures (d) dark and (e) hashed. Note, Z is the compression axis during SPS.

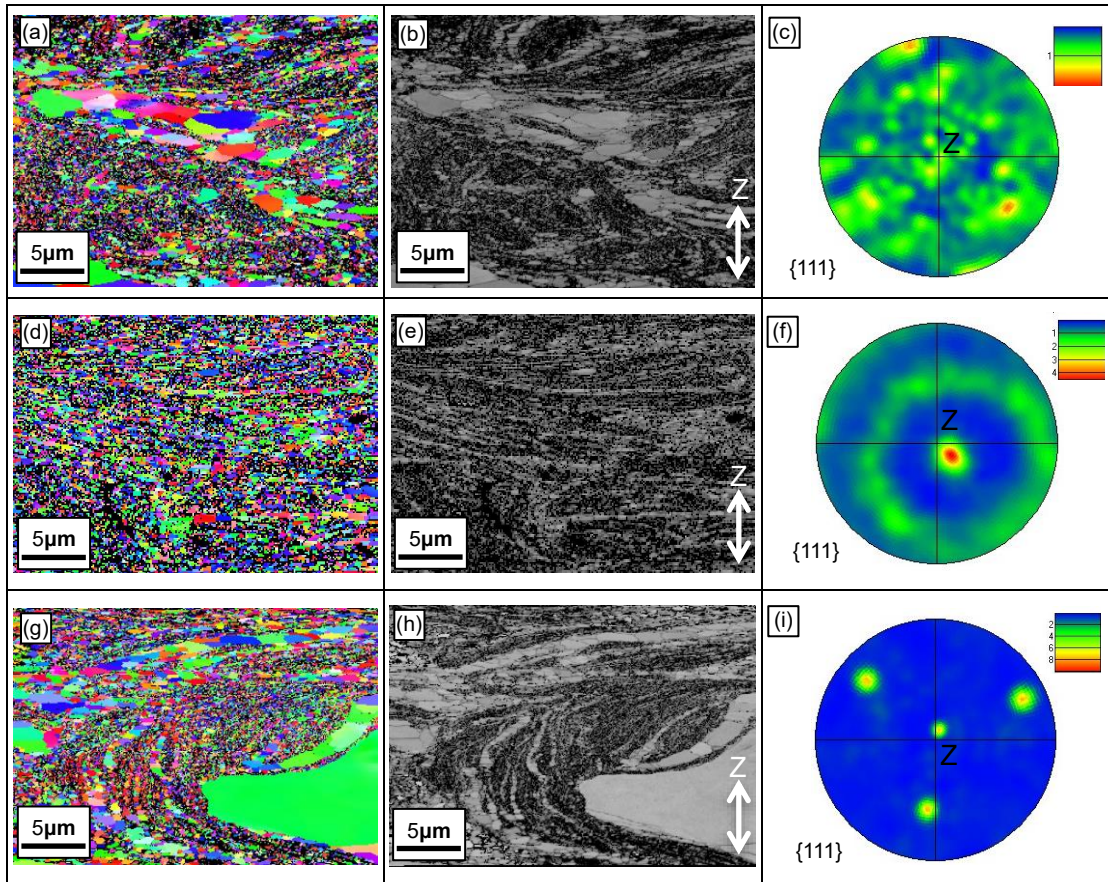


Figure 4. EBSD data of heat treated material. (a) (d) (g) IPF maps of material heat treated to 800, 1000 and 1200°C, respectively. (b) (e) (h) band contrast maps of maps (a), (d) and (g), respectively. (c) (f) (i) {111} pole figures of maps (a), (d) and (g), respectively. Note, Z is the compression axis during SPS.